Crystal Structures of Ferrous and CO-, CN^--, and NO-Bound Forms of Rat Heme Oxygenase-1 (HO-1) in Complex with Heme: Structural Implications for Discrimination between CO and O_2 in HO-1[†,‡]

Masakazu Sugishima,[§] Hiroshi Sakamoto,*[,||] Masato Noguchi,[||] and Keiichi Fukuyama*[,§]

Department of Biology, Graduate School of Science, Osaka University, Toyonaka, Osaka 560-0043, Japan, and Department of Medical Biochemistry, Kurume University School of Medicine, 67 Asahi-machi, Kurume 830-0011, Japan

Received December 2, 2002; Revised Manuscript Received June 16, 2003

ABSTRACT: Heme oxygenase (HO) catalyzes heme degradation by utilizing O_2 and reducing equivalents to produce biliverdin IXα, iron, and CO. To avoid product inhibition, the heme−HO complex (heme−HO) is structured to markedly increase its affinity for O_2 while suppressing its affinity for CO. We determined the crystal structures of rat ferrous heme−HO and heme−HO bound to CO, CN^-, and NO at 2.3, 1.8, 2.0, and 1.7 Å resolution, respectively. The heme pocket of ferrous heme−HO has the same conformation as that of the previously determined ferric form, but no ligand is visible on the distal side of the ferrous heme. Fe−CO and Fe−CN^- are tilted, whereas the Fe−NO is bent. The structure of heme−HO bound to NO is identical to that bound to N_3^-, which is also bent as in the case of O_2. Notably, in the CO- and CN^--bound forms, the heme and its ligands shift toward the α-*meso* carbon, and the distal F-helix shifts in the opposite direction. These shifts allow CO or CN^- to bind in a tilted fashion without a collision between the distal ligand and Gly139 O and cause disruption of one salt bridge between the heme and basic residue. The structural identity of the ferrous and ferric states of heme−HO indicates that these shifts are not produced on reduction of heme iron. Neither such conformational changes nor a heme shift occurs on NO or N_3^- binding. Heme−HO therefore recognizes CO and O_2 by their binding geometries. The marked reduction in the ratio of affinities of CO to O_2 for heme−HO achieved by an increase in O_2 affinity [Migita, C. T., Matera, K. M., Ikeda-Saito, M., Olson, J. S., Fujii, H., Yoshimura, T., Zhou, H., and Yoshida, T. (1998) *J. Biol. Chem. 273,* 945−949] is explained by hydrogen bonding and polar interactions that are favorable for O_2 binding, as well as by characteristic structural changes in the CO-bound form.

Heme oxygenase (HO,[1] EC 1.14.99.3) is a microsomal enzyme which regiospecifically cleaves the porphyrin ring of heme at the α-*meso* carbon, producing biliverdin IXα, iron, and CO (*1*). To date, HO is the only known CO-producing enzyme in mammals. Its structure in complex with heme (heme−HO) consists mainly of α-helices (*2*−*4*) with heme sandwiched between the proximal (A-helix, Leu13−Glu29) and distal kinked (F-helix, Leu129−Met155) helices. Our recent study of the heme-free form of HO showed that the A-helix is disorderd and the F-helix fluctuates. We proposed an induced-fit model for heme binding to HO (*5*). The amino acid sequence in the F-helix, the "heme oxygenase signature" (*6*), is highly conserved in all HOs. No dissociable residue is present on the distal side of the heme in heme−HO. The closest residue is Gly143, and its amide group is hydrogen bonded to H_2O or to OH^- coordinated to the heme iron (*2*−*4*). On the basis of the structure of the azide-bound form of heme−HO (N_3^-−heme−HO), we recently suggested that Gly143 and a hydrogen bonding solvent network on the distal side play a major role in the regiospecific hydroxylation of heme at the α-*meso* carbon during the HO reaction (*7*).

The CO produced in the HO reaction may be a product inhibitor. Indeed, heme degradation never occurs under a CO atmosphere. Moreover, the reaction stops at the step of verdoheme, the second intermediate in the HO reaction, under a gas phase of 20% CO and 80% O_2 (*8*). The CO produced by HO, however, seems never to interfere with *in vitro* heme degradation by HO under a very low CO concentration as in the atmosphere. Conceivably, the active site of HO may be equipped with a variety of structural

[†] This work was supported in part by Grants-in-Aid for Scientific Research on Priority Areas (Biological Machinery) to K.F. (Grant 11169223) and M.N. (Grant 13033041), by a Grant-in-Aid for Scientific Research (C) to M.N. (Grant 12670125) from the Ministry of Education, Culture, Sports, Science, and Technology of Japan, by a Grant-in-Aid for The Science Research Promotion Fund from The Promotion and Mutual Corporation for Private Schools of Japan to M.N., and by Grant 00K1100 from the Ichiro Kanehara Foundation to H.S.

[‡] Coordinates have been deposited in the Protein Data Bank as entries 1IX4 (CO−heme−HO), 1IX3 (CN^-−heme−HO), 1J02 (NO−heme−HO), and 1UBB (ferrous heme−HO).

* To whom correspondence should be addressed. K.F.: phone, +81-6-6850-5422; fax, +81-6-6850-5425; e-mail, fukuyama@bio.sci.osaka-u.ac.jp. H.S.: phone, +81-942-31-7544; fax, +81-942-31-4377; e-mail, sakamoto@med.kurume-u.ac.jp.

[§] Osaka University.

[||] Kurume University School of Medicine.

[1] Abbreviations: HO, heme oxygenase; heme−HO, HO-1 in complex with heme; N_3^-−heme−HO, ferric heme−HO-1 bound to azide; CO−heme−HO, ferrous heme−HO-1 bound to carbon monoxide; CN^-−heme−HO, ferric heme−HO-1 bound to cyanide; NO−heme−HO, ferrous heme−HO-1 bound to nitric oxide; Mb, myoglobin.

10.1021/bi027268i CCC: $25.00 © 2003 American Chemical Society
Published on Web 08/02/2003

devices that allow HO to escape inhibition by locally produced CO.

The affinities of ligands such as CO and O_2 for the heme iron in hemoproteins vary markedly depending on the heme environment. For free heme in organic solvents, the ratio of the affinities of CO and O_2 for the heme iron, the ratio of the CO equilibrium constant (K_{CO}) to the O_2 equilibrium constant (K_{O_2}), is ~30000−100000 (*9*, *10*), whereas in myoglobin (Mb), $K_{CO}/K_{O_2} = 25-41$ (*10*). A number of structural analyses of oxy- and carbonmonoxy-Mb have shown that the discrimination between CO and O_2 by Mb is primarily due to hydrogen bonding and other polar interactions rather than steric hindrance (*10*−*16*). Neutron diffraction crystallographic analysis of both forms of Mb indicates that on O_2 binding to the heme in Mb, the Nϵ atom of the distal histidine (HisE7) is protonated and O_2 forms a hydrogen bond with HisE7 (*12*), whereas HisE7 Nδ is protonated on CO binding (*13*). Recent site-directed mutagenesis and spectroscopic analyses, however, suggest that HisE7 Nϵ is protonated and hydrogen bonded to the distal ligand in both ligand-bound forms (*14*, *15*). If so, the electrostatic field calculation of the heme pocket of Mb indicates good correlations between the electrostatic potentials of the distal ligand, the stretching frequencies of IR and Raman resonance, and the dissociation rate constants of both ligands in wild-type and mutant Mbs (*16*). Distal pocket polarity therefore would be a key for discrimination between polar O_2 and apolar CO in Mb.

Studies of O_2 and CO reactions with heme−HO, as compared with those of Mb, reported by Ikeda-Saito and co-workers (*17*), seem exceedingly important; O_2 affinities are very high ($K_{O_2} = 30-80\ \mu M^{-1}$), 30−90-fold greater than those for Mb. The O_2 association rate constants are similar to those for Mb ($k'_{O_2} = 7-20\ \mu M^{-1}\ s^{-1}$), whereas O_2 dissociation rate constants are remarkably slow ($k_{O_2} = 0.25\ s^{-1}$), which suggests the presence of favorable interactions between the bound O_2 and protein residues in the heme pocket. Such interactions between the distal residues in HO and the bound O_2 have been proposed on the basis of ESR findings (*18*). In contrast, the CO affinity of heme−HO is reported to be similar to that of Mb (*17*). CO binding to the heme bound to HO is biphasic. The respective K_{CO}/K_{O_2} ratios are 5.4 and 1.2 for the fast and slow phases, respectively. Thus, HO discriminates much more strongly against CO binding with increased affinity for O_2 than Mb does.

In the study presented here, we have determined the crystal structures of the reduced form of rat HO-1 in complex with heme (ferrous heme−HO) (2.3 Å) and the complexes bound to CO (CO−heme−HO) (1.8 Å), CN^- (CN^-−heme−HO) (2.0 Å), and NO (NO−heme−HO) (1.7 Å). CN^-, an inhibitor of HO catalysis (*19*), is considered a CO analogue in terms of a similar mode of binding of CN^- to heme iron as observed in other hemoproteins. We present a structural basis that explains the conspicuously high O_2 affinity in heme−HO, as well as the strong discriminating mechanism of HO against CO as compared to Mb.

EXPERIMENTAL PROCEDURES

Preparation of Ferrous Heme−HO and Ligand-Bound Crystals. The expression and purification of truncated rat HO-1 (Met1−Pro267), as well as the preparation of its complex with heme, are described elsewhere (*7*, *20*, *21*). Ferric heme−HO was crystallized under conditions similar to those for N_3^-−heme−HO with a microcrystal of N_3^-−heme−HO as the seed. Ferrous heme−HO crystals were prepared by soaking ferric heme−HO crystals in an anaerobic solution containing an excess of sodium dithionite. On reduction, the crystal color immediately became bright red. CN^-−heme−HO was prepared by adding potassium cyanide to a ferric heme−HO solution for a final concentration of 10 mM, and crystallized under the same conditions that were used for N_3^-−heme−HO (*7*), the protein concentration being 40 mg/mL in 50 mM potassium phosphate buffer (pH 7.0) containing 10 mM potassium cyanide. The CO−heme−HO crystal was prepared by soaking an N_3^-−heme−HO crystal in a CO-saturated solution until the crystal became bright red (30 min to 2 h). The CO-saturated solution was prepared just before the crystals were soaked; sodium ascorbate at a final concentration of 100 mM was added to the crystallization solution, and then two cycles of alternate degassing (15 m) and CO bubbling (5 m) were carried out. The NO−heme−HO crystal was prepared by soaking the N_3^-−heme−HO crystal in an NO-saturated solution. The crystal immediately became bright red. The NO-saturated solution was prepared just before the crystals were soaked. Sodium dithionite and NOC-12, an NO donor (Dojindo, Kumamoto, Japan), were added in excess to the crystallization solution, the gas phase of which had been replaced with N_2 in advance by two cycles of alternate degassing (15 min) and an N_2 purge (5 min). The ferrous heme−HO, CO−heme−HO, and NO−heme−HO crystals on the cryoloop were immediately cooled with liquid nitrogen. The CN^-−heme−HO crystal was soaked for a few seconds in a crystallization solution that contained 50 mM potassium cyanide, and then the crystal on the cryoloop was flash-cooled under a nitrogen gas stream at 100 K. The CN^-−heme−HO crystals became bright red when they were soaked in 50 mM potassium cyanide (final pH of 9.2).

Data Collection and Processing. Diffraction data for the ferrous heme−HO crystal were collected at 100 K with an FR-D rotating anode X-ray generator ($\lambda = 1.5418$ Å) and an R-AXIS IV^{++} imaging plate system (RIGAKU). Its crystal was oscillated by 1.5° per frame at an exposure time of 20 min and a total measurement angle of 120°. Diffraction data for CN^-−heme−HO were collected at 100 K using synchrotron radiation ($\lambda = 1.000$ Å) at beamline BL40B2 of SPring-8 and an ADSC Quantum 4R detector. Its crystal was oscillated by 1.5° per frame at an exposure time of 120 s and a total measurement angle of 60°. Diffraction data for CO−heme−HO and NO−heme−HO were collected at 100 K using synchrotron radiation ($\lambda = 1.000$ Å) at beamline BL41XU of SPring-8 and a MarCCD system. For CO−heme−HO, the crystal was oscillated by 1.5° per frame at an exposure time of 5 s and a total measurement angle of 180°. To measure intensities of the overloaded diffractions, the X-ray beam was attenuated to 7%, and then the same crystal was oscillated by 3.0° per frame with a 3 s exposure. The two data sets were scaled and merged using 50−1.8 Å data for the former and 50−3.5 Å data for the latter. For NO−heme−HO, the exposure time per frame was 6 s and the total measurement angle was 120°. To collect low-resolution data, the X-ray beam was attenuated to 25%, and then intensity data were collected under the same conditions

Table 1: Summary of Crystallographic Statistics

	ferrous heme−HO	CO−heme−HO	CN^-−heme−HO	NO−heme−HO
space group	$P3_221$	$P3_221$	$P3_221$	$P3_221$
$a = b$ (Å)	65.3	66.0	65.7	65.4
c (Å)	120.5	120.2	119.7	121.1
resolution (Å)	50−2.3	50−1.8	50−2.0	50−1.7
no. of unique reflections	13787	28853	20629	32251
redundancy	6.4	11.8	3.5	9.5
completeness (%)[a]	99.9 (99.9)	99.7 (97.4)	99.3 (99.3)	99.8 (99.5)
R_{merge}[a,b]	0.102 (0.347)	0.067 (0.315)	0.066 (0.284)	0.052 (0.346)
R/R_{free}[c,d]	0.186/0.220	0.195/0.214	0.198/0.223	0.201/0.227
rms deviation from ideality				
bonds (Å)	0.006	0.005	0.006	0.005
angles (deg)	1.14	1.24	1.19	1.12
average B-factors (Å^2)				
main chain	24.7	23.5	23.7	26.5
side chain	27.2	27.2	26.8	29.5
solvent	35.6	36.7	34.2	39.6
heme	26.7	27.3	24.8	30.7
distal ligand	−	24.3	20.6	32.8

[a] Values in parentheses are for the outermost shell: 2.42−2.30 Å for ferrous heme−HO, 1.86−1.80 Å for CO−heme−HO, 2.07−2.00 Å for CN^-−heme−HO, and 1.76−1.70 Å for NO−heme−HO. [b] $R_{merge} = \sum_{hkl}\sum_i|I_i(hkl) - \langle I(hkl)\rangle|/\sum_{hkl}\sum_i I_i(hkl)$. [c] $R = \sum|F_o(hkl) - F_c(hkl)||/\sum|F_o(hkl)|$. [d] R_{free} values are R values calculated for 5% (ferrous heme−HO and NO−heme−HO) and 10% (CO−heme−HO and CN^-−heme−HO) of the data set not included in refinements.

that were used for CO−heme−HO. The two data sets were scaled and merged using 50−1.7 Å data for the former and 50−3.5 Å data for the latter. These diffraction data were processed, merged, and scaled with MOSFLM (*22*) and SCALA (*23*, *24*) for the ferrous heme−HO and CN^-−heme−HO and with HKL2000 (*25*) for CO−heme−HO and NO−heme−HO. Crystallographic data and diffraction statistics are given in Table 1.

Model Building and Refinement. Because the CN^-−heme−HO crystal was isomorphous with the N_3^-−heme−HO crystal (*7*), its structure was determined by applying rigid body, simulated annealing, and temperature factor refinements to the structure of its protein moiety using 50.0−2.5 Å resolution data. The structure was revised by alternate adjustment of the model with XtalView (*26*) and simulated annealing and temperature factor refinements using 50.0−2.0 Å resolution data. The heme, clearly present in the electron density map, was included in subsequent refinement. After a few cycles of water picking and energy minimization refinements, the electron density for the stretch of Glu234−Leu243 appeared as a separate density, and its model was included in subsequent refinement. Last, the cyanide ion was located in the $F_o - F_c$ map and included in the energy minimization refinement, in which neither the Fe···C−N^- angle nor the Fe···C distance was restrained. The structures of ferrous heme−HO, CO−heme−HO, and NO−heme−HO were refined by the same procedures using 50.0−2.3, 50.0−1.8, and 50.0−1.7 Å resolution data, respectively. All the refinements were done with CNS (*27*). Stereochemical checks of the models were done with PROCHECK (*23*, *28*). Refinement statistics are given in Table 1.

RESULTS

Overall Structures. The structures of the ferrous heme−HO, CO−heme−HO, CN^-−heme−HO, and NO−heme−HO have been refined at 2.3 Å resolution to R and R_{free} values of 0.186 and 0.220, at 1.8 Å resolution to R and R_{free} values of 0.195 and 0.214, at 2.0 Å resolution to R and R_{free} values of 0.198 and 0.223, and at 1.7 Å resolution to R and R_{free} values of 0.201 and 0.227, respectively. In CN^-−heme−HO, the C-terminal loop (Glu234−Leu243) has become ordered, but the side chains of Glu234 and Arg237 are still disordered. This loop is located at the back of the heme pocket. The distance (30 Å) between Thr222 and Glu234 indicates that the disordered segment (Glu223−Thr233) assumes an extended conformation. The side chain of Lys177 is disordered in each of the CO−, CN^-−, and NO−heme−HO crystals. In CO−heme−HO and NO−heme−HO, the side chain of Glu190 is disordered. In CO−heme−HO, the side chains of Glu19 and Glu45 are also disordered. In NO−heme−HO, there are several alternate conformations for the side chains on the molecular surface and an additional NO molecule near the side chain of Arg27. In N_3^-−heme−HO, an additional azide molecule was also found to bind to the same site (*7*). In the ferrous heme−HO structure, no electron density is present on the distal side of the heme iron, consistent with previous spectroscopic findings (*29*−*31*).

Structural comparisons of the various forms of heme−HO are shown in Figure 1. The overall structure of ferrous heme−HO is identical to that of N_3^-−heme−HO (*7*) (Figure 1a) and similar to that of ferric heme−HO (*3*), the root-mean-square (rms) deviations for the Cα atoms being 0.13 and 0.46 Å, respectively. The relatively large rms deviation between the ferrous and ferric heme−HO forms is mainly due to the different conformations in the F−G and G−H loops on the molecular surface; the rms deviation is 0.28 Å when these loops are excluded. The space groups of the ferrous and ferric heme−HO crystals differ, and these loops are involved in intermolecular contacts. The structural difference in these loops therefore would be due to the crystal packing force. NO−heme−HO also has the same structure as ferrous heme−HO (Figure 1a), the rms deviation being 0.13 Å. The heme position remains unchanged on NO binding to the ferrous iron as it does on N_3^- binding to the ferric iron (*7*). It may be concluded that neither the oxidation state of the heme iron nor substitution of the distal ligand of heme−HO with NO or N_3^- affects the HO structure.

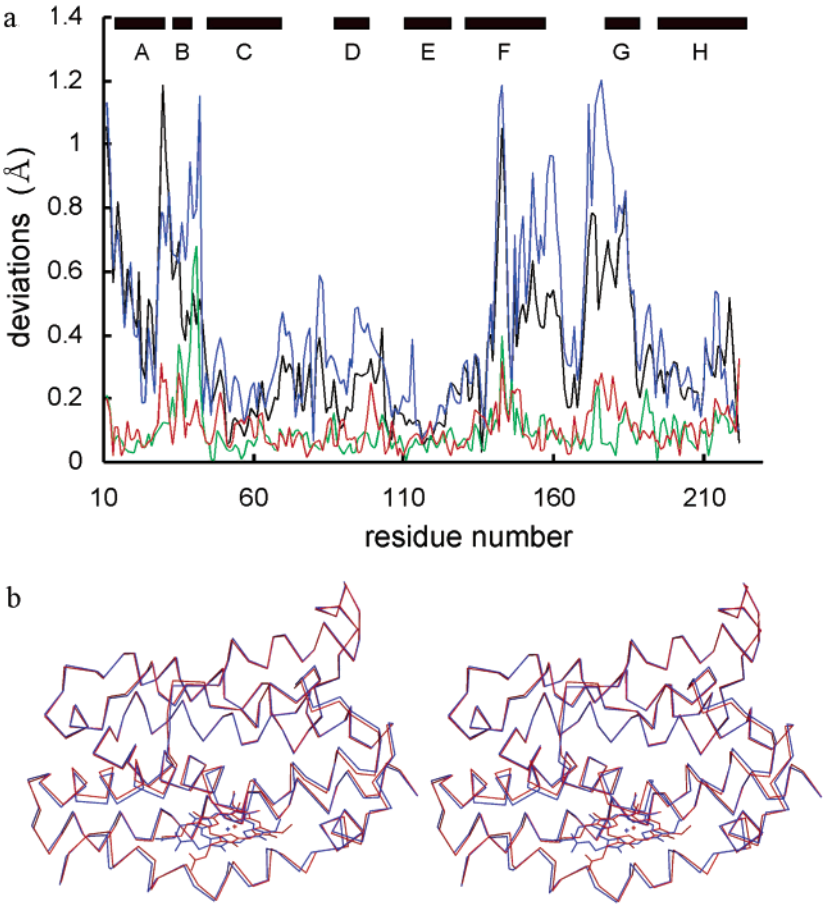

FIGURE 1: Structural comparisons of various forms of heme-HO. (a) Plots of Cα atom deviations between ferrous heme−HO and ligand-bound heme−HOs: N_3^-−heme−HO (red), NO−heme−HO (green), CO−heme−HO (black), and CN^-−heme−HO (blue). Solid horizontal bars represent the helices in the ferric heme−HO (*3*). (b) Stereodiagram of Cα traces of ferrous heme−HO (blue) and CO−heme−HO (red). The models are superimposed to minimize the rms deviation of the corresponding Cα atoms of all the amino acid residues. This figure was prepared with MOLSCRIPT (*45*) and Raster3D (*46*).

Superimposition of the ferrous heme−HO and CO−heme−HO structures (Figure 1b) shows that on CO binding the heme shifts (0.9 Å) toward the α-*meso* carbon along the α−γ axis of the heme. The plot of deviations for Cα atoms between ferrous heme−HO and CO−heme−HO (Figure 1a) shows marked differences in the positions of the A-, B-, F-, and G-helices which constitute the heme binding site of HO. In CO−heme−HO, the proximal A-helix and following B-helix move in the direction of the α-*meso* carbon together with the heme shift, whereas the distal F- and G-helices shift in the opposite direction; e.g., the Cα atoms of His25 in the A-helix and Gly143 in the F-helix are located 0.5 and 1.1 Å, respectively, from their positions in the ferrous heme−HO. Because no significant structural change occurs in the heme pocket on NO binding to the ferrous heme, these heme shift and conformational changes on CO binding can be attributed to the difference in the coordination modes of the ligands.

The structure of CN^-−heme−HO, as compared with that of the ferrous heme−HO, also shows large deviations at residues located in the heme pocket (Figure 1a). It is similar to the structure of CO−heme−HO; the rms deviation for Cα atoms between the CO- and CN^--bound forms is 0.29 Å. The heme shift, accompanied by movement of the A- and B-helices, in the α-*meso* direction, and repositioning of the F- and G-helices occur in CN^-−heme−HO as they do in CO−heme−HO. If the ferric state of the heme iron in CN^-−heme−HO is taken into account, it is conceivable that the binding modes of CO and CN^-, not the redox states of the heme iron, are responsible for these conformational changes.

Ligand Coordination Modes. In the $F_o - F_c$ map of CO−heme−HO, the ellipsoidal density on the distal side of the heme iron, which can be assigned to the CO molecule, is tilted toward the α-*meso* carbon (Figure 2a). The Fe···C−O angle has converged to 158° and the Fe···C distance to 2.0 Å by refinement. This tilt geometry is comparable to the Fe···C−O angle (∼160°) obtained by infrared measurements (*10*) and recent high-resolution X-ray analysis (*11*) for CO-bound Mb. Due to repositioning of the heme and distal helix, the distance between Gly143 N and the carbon atom of CO is lengthened to 3.5 Å in comparison to the close contact (2.8 Å) between Gly143 N and the iron-bound nitrogen atom of the azide in N_3^-−heme−HO (*7*). The oxygen atom of CO is in van der Waals contact with Gly139 O (2.9 Å) and Gly144 N (3.1 Å). In the distal pocket of CO−heme−HO, the five ordered water molecules present in heme−HO (*2*−*4*) and N_3^-−heme−HO (*7*) are conserved. These water molecules are involved in the hydrogen bonding network that may be important for catalyzing hydroxylation of the α-*meso* position of heme (*32*, *33*). One of these ordered water molecules is located 2.9 Å from the oxygen atom of CO.

CN^- is coordinated to the heme iron in the same mode as CO; the Fe···C−N angle is 166° and the Fe···C distance

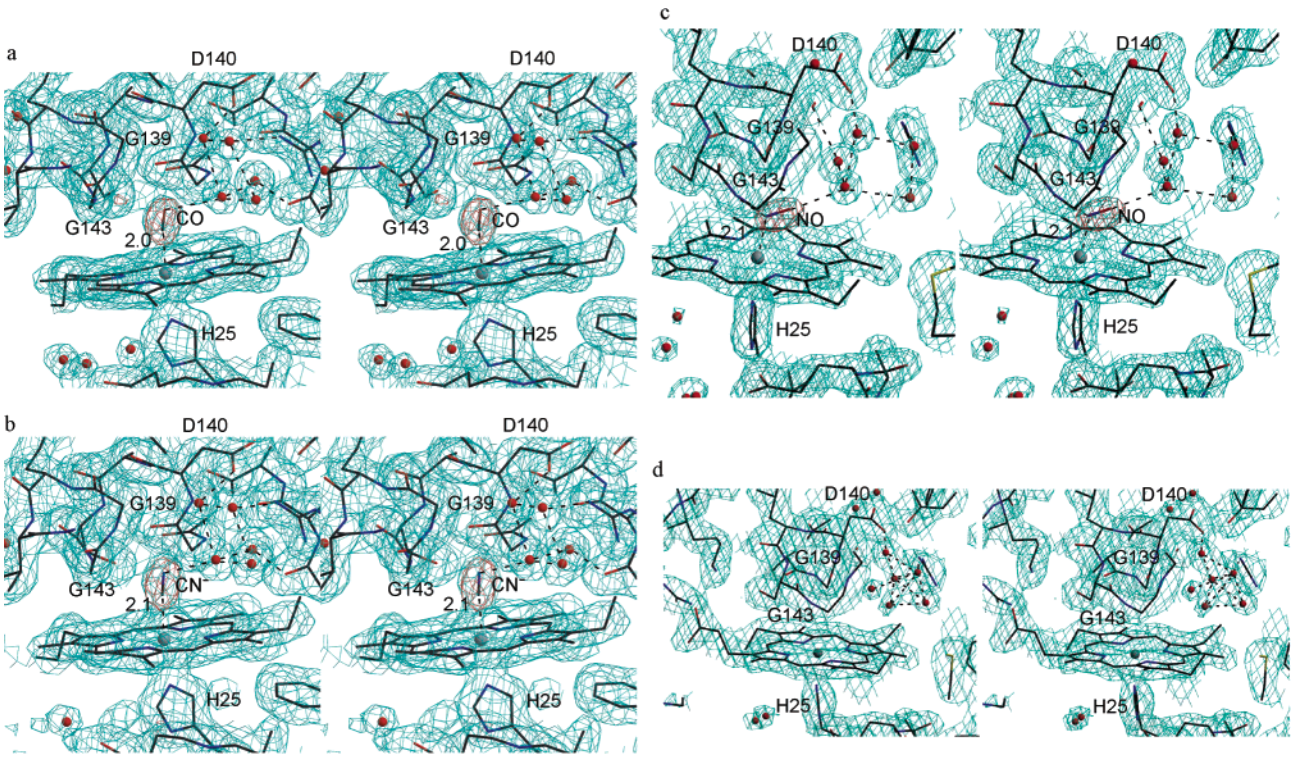

FIGURE 2: Structures of CO−heme−HO, CN^-−heme−HO, NO−heme−HO, and ferrous heme−HO around the heme pockets. σ_A-weighted $2F_o - F_c$ (cyan) and $F_o - F_c$ (red) maps superimposed on the wire-frame model are shown in stereoview. Dashed lines show the hydrogen and coordination bonds involved in stabilization of distal ligand binding: (a) CO−heme−HO, (b) CN^-−heme−HO, (c) NO−heme−HO, and (d) ferrous heme−HO. Each $2F_o - F_c$ map is contoured at 1.2σ, whereas the $F_o - F_c$ map at 5.0σ was calculated by omitting the exogenous ligand bound to the heme iron. Fe···C(CO) and Fe···C(CN^-) distances are in angstroms. This figure was prepared with MOLSCRIPT (*45*), Raster3D (*46*), and CONSCRIPT (*47*).

2.1 Å (Figure 2b). The tilt angle (~20°) and direction of CN^- are roughly consistent with the magnetic axis determined by NMR spectroscopy for human CN^-−heme−HO (*34*). Cyanide anion is accommodated in the heme pocket in a manner similar to that of the CO in CO−heme−HO. The iron-bound carbon atom of CN^- is 3.6 Å from Gly143 N, whereas the terminal nitrogen atom is in van der Waals contact with Gly139 O (2.8 Å) and Gly144 N (2.8 Å). A hydrogen bonding network is also present in CN^-−heme−HO, and the distance between CN^- and the nearest water molecule is 2.6 Å.

In contrast, in NO−heme−HO, NO is bent toward the α-*meso* carbon of the heme; the Fe···N−O angle has converged to 125° and the Fe···N distance to 2.1 Å by refinement (Figure 2c). This bent geometry is comparable to the coordination of azide to the heme iron in N_3^-−heme−HO, in which the corresponding angle is 116° and the distance is 2.2 Å (*17*), and also similar to that of NO in NO-bound Mb, in which the corresponding angle is 112 ± 5° and the distance is 1.9 Å (*35*). The nitrogen atom of NO is hydrogen bonded to Gly143 N (2.8 Å) and in a van der Waals interaction with Gly139 O (2.9 Å) as is the iron-bound nitrogen of azide in N_3^-−heme−HO. The oxygen atom of NO is 2.8 Å from Gly139 O, 3.2 Å from Gly144 N, and 2.9 Å from a water molecule in the hydrogen bonding network.

Water molecules in such a distal hydrogen bonding network are also present in ferrous heme−HO, but the distal ligand is lacking (Figure 2d). Electron density for five of the six water molecules in this hydrogen bonding network is broad (Figure 2d), indicative of fluctuation.

Interactions of Propionate Groups with Basic Residues in the Heme Pocket. The current structures of the various ligand-binding forms of heme−HO show that the binding modes of ligands affect the electrostatic interactions of the propionate groups of the heme with side chains that have important roles for the correct accommodation of heme in the active site (*2*, *3*). Lys18, Lys179, and Arg183 are clustered near the propionate groups in the ferric (*2*, *3*) and ferrous heme−HO complexes and in N_3^-−heme−HO (*7*). The structures of these basic residues are unaffected by the bound NO. The side chains of Lys179 in CO−heme−HO and Lys18 in CN^-−heme−HO, however, have different conformations and no longer interact with the propionates (Figure 3). The refinement for NO−heme−HO, at present, includes only the major orientation of heme, though additional electron density of the heme is observed as in N_3^-−heme−HO; the heme has two orientations related to each other by a 180° rotation about the α−γ axis. One propionate group exposed to solvent has two conformations, both of which are directed to the distal side. Dual orientations and conformations are not seen in this X-ray analyses of CO− and CN^-−heme−HO. On the basis of NMR analysis (*34*), however, there are two orientations of heme in CN^-−heme−HO. The propionate exposed to solvent is directed toward the proximal side in CO− and CN^-−heme−HO. In addition, the α−γ axis of the heme in CO− and CN^-−heme−HO is slightly rotated along the axial axis as compared to the α−γ axis in N_3^-−heme−HO. Consequently, the δ-*meso* carbon and propionate group are more exposed to the solvent.

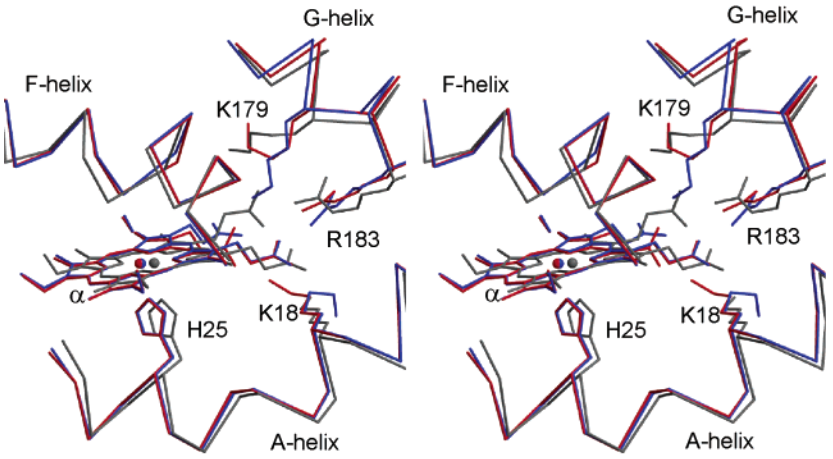

FIGURE 3: Structural changes on CO binding. Stereodiagram around the heme pockets of CO−heme−HO (red), CN^-−heme−HO (blue), and ferrous heme−HO (gray). The models are superimposed to minimize rms deviations of the Cα atoms of all the amino acid residues. The A-, F-, and G-helices are shown as Cα traces and Lys18, His25, Lys179, Arg183, heme, CO, and CN^- as a wire-frame model. This figure was prepared with MOLSCRIPT (*45*) and Raster3D (*46*).

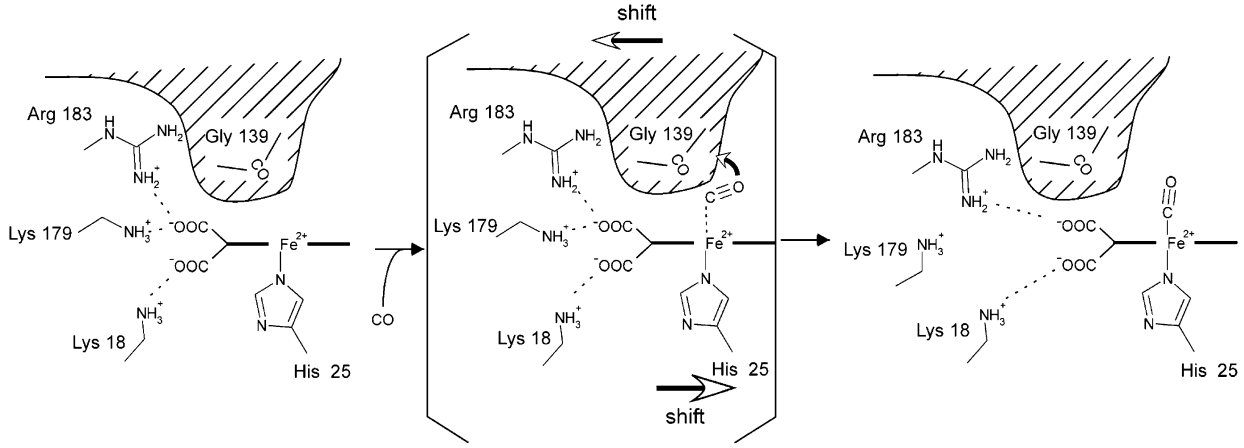

FIGURE 4: Possible model for CO coordination to the heme iron.

DISCUSSION

The most notable feature of CO and CN^- binding to the heme bound to HO is gross relocation of the active site accompanied by a heme shift. Although a heme shift on ligand binding has been reported in dimeric clam hemoglobin, it is involved in cooperative ligand binding through residues on the subunit interface that link the heme of one subunit to the proximal helix of the second subunit (*36*). The tilting geometry of CO or CN^- in the distal pocket of heme−HO would produce steric hindrance between CO or CN^- and the distal helix, if the locations of both the protein and heme remain unchanged; the oxygen atom of CO or the nitrogen atom of CN^- would collide with Gly139 O (2.0 Å). To avoid such steric hindrance, the heme and its ligands shift along the $\alpha-\gamma$ axis of the heme, and the distal F-helix shifts in the opposite direction. These shifts accompany the G-helix shift. Such structural changes disrupt the salt bridge between the heme and protein in heme−HO (Figure 3). Most likely, gross structural change is induced by ligands such as CO which coordinates to the heme in HO in a tilt manner, as shown in Figure 4.

Recent NMR studies of the CN^--bound forms of human HO in complexes with heme (*34*) and its symmetric derivative (*37*) show that the central portion of the distal helix is closer to the heme in the solution structure than it is in the crystal structure of human heme−HO, with the position in solution more closely resembling that in the crystal structure of rat heme−HO. The likely movement of the distal helix by ∼0.5 Å closer to the heme iron (*37*) is consistent with a difference in the positions of the distal helix of the crystal structures of rat and human HOs. The distance between Gly143 N and the heme iron is 4.9 Å in rat CN^-−heme−HO in this study, whereas the distances in the two molecules of human heme−HO in an asymmetric unit (*2*) are 5.3 and 6.0 Å. NMR studies also show that the four-ring aromatic cluster (Tyr58, Tyr137, Phe166, and Phe167) moves closer to the heme, but no rearrangement of the aromatic cluster occurs in rat heme−HO on the binding of various ligands, including CN^-.

Unlike CO and CN^-, NO coordinates to the heme iron in a bent geometry in NO−heme−HO as does N_3^- in N_3^-−heme−HO (*17*). NO binding to heme−HO causes no significant change in the conformation of the heme binding site or in the heme position. With respect to the Fe···N−O angles in the model heme compounds, there are three types depending on the number of metal d-electrons plus the electron in the π^* orbitals of NO (*38*, *39*): ∼180° in six (ferric heme−NO), ∼140° in seven (ferrous heme−NO), and ∼120° in eight. In NO−heme−HO, as in NO-bound Mb (*35*), NO is more bent compared to the ideal geometry,

indicative of an increased level of π-bonding between the heme iron and NO. O_2 also prefers a bent geometry; a previous resonance Raman study of the oxygenated form of heme−HO revealed that bound O_2 assumes a bent geometry with an Fe−O−O angle of ~110° (*40*). NO−heme−HO, as well as N_3^-−heme−HO, therefore, would be a suitable analogue for examining the binding mode of O_2 and dioxygen activation in the HO reaction. On account of the α-*meso* orientation of NO, the oxygen atom of NO is in close contact with the α-*meso* carbon (3.5 Å), suggesting that the distal oxygen atom of hydroperoxide, the active oxygen species for α-*meso* hydroxylation, can easily attack the α-*meso* carbon directly.

Generally, the main factors regulating the CO and O_2 affinities of a hemoprotein are the shape of the heme pocket (steric hindrance), hydrogen bonds, and the polarity of the heme pocket (*41*). Studies for O_2 and CO binding to heme analogues aimed at evaluating these three effects have shown that steric hindrance that bends the Fe···CO bond decreases the binding affinity for CO, whereas the affinity for O_2 is unaffected. Hydrogen bonding to the distal ligand and the polarity in the heme pocket, however, increase the binding affinity for O_2, whereas the affinity for CO is unaffected (*41*). In the case of HO, strict discrimination between O_2 and CO is mainly brought about by an increase in O_2 affinity that is characterized by a remarkably slow O_2 dissociation rate constant (*17*). Comparison of the distal environments of the CO- and NO-bound forms clearly shows that the hydrogen bond between Gly143 N and NO is present in a bent geometry, but such an interaction is no longer seen in the tilt geometry (Figure 5). Although the biochemical data for the affinity for NO of ferrous heme−HO are not available, its affinity for ferric heme−HO was reported to be higher than that of met-Mb (*42*). The affinity of binding of NO to the iron atom of hemoproteins is generally much higher in the ferrous state than in the ferric state (*43*, *44*). In addition, NO binding is stabilized by the hydrogen bond to water (Figure 2c). Its affinity for ferrous heme−HO would be greater than that of Mb. Because of the highly bent structure for O_2 coordination, Gly143 N would form a hydrogen bond with the iron-bound oxygen atom of O_2, which would stabilize the coordination of O_2 to the heme iron, thereby decreasing the O_2 dissociation rate constant. Consequently, we conclude that it is the hydrogen bonding of Gly143 N with O_2 which primarily controls ligand discrimination by HO.

Moreover, a series of polar interactions may increase the binding affinity for O_2 of HO. Gly139 O and Gly144 N are in van der Waals contact with the ligands in both coordination geometries, indicating that these polar groups may exert a preference for a polar O_2 over an apolar CO. One of the ordered water molecules in the distal hydrogen bonding network is also located within 3 Å of the distal ligands in both geometries. This hydrophilic network has the ability to donate hydrogen to the heme ligand, and some have speculated that the network is essential for catalyzing hydroxylation of the α-*meso* position of heme (*7*, *32*, *33*). The polarity of this network also probably contributes to the increase in the binding affinity for O_2 of heme−HO. For tilt-type ligands such as CO, however, the stabilization gained by the hydrogen bond between the terminal atom of the ligand and one of the water molecules in the conserved network may be canceled, at least in part, by the disruption of the salt bridge between the heme propionate and basic residue caused by the heme shifts (Figure 3). This may result in the affinity for CO in HO being comparable to that in Mb.

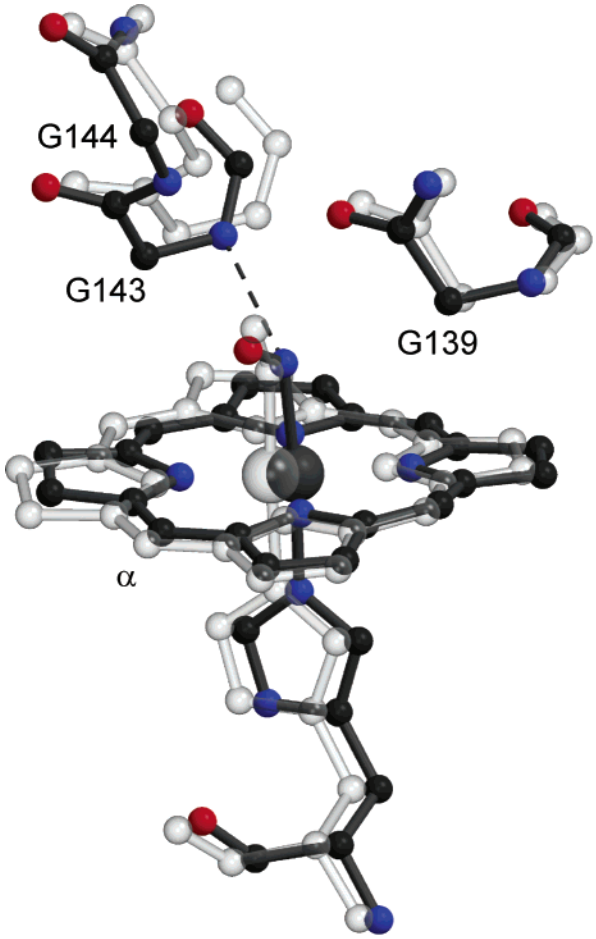

FIGURE 5: Superimposition of the heme distal sides of CO−heme−HO and NO−heme−HO. Ball-and-stick model for heme, ligands, Gly139, Gly143, and Gly144 of NO−heme−HO (carbon and iron are black, nitrogen is blue, and oxygen is red) superimposed on that of CO−heme−HO (transparent light gray). The dashed line represents the hydrogen bond between Gly143 N and the nitrogen atom of NO in NO−heme−HO. The porphyrin substituents are omitted for clarity. This figure was prepared with MOLSCRIPT (*45*) and Raster3D (*46*).

ACKNOWLEDGMENT

We thank Drs. Keiko Miura, Hisanobu Sakai, and Masahide Kawamoto of the Japan Synchrotron Radiation Research Institute (JASRI) for their valuable help with data collection using synchrotron radiation at BL40B2 and BL41XU, SPring-8. We also thank Dr. Yoshimitsu Kakuta (Kyushu University, Kyushu, Japan) for his advice on the biochemical and crystallographic work. Synchrotron radiation experiments were performed with the approval of JASRI (2001B0659-RL-np and 2002A0699-RL-np).

REFERENCES

1. Tenhunen, R., Marver, H. S., and Schmid, R. (1968) *Proc. Natl. Acad. Sci. U.S.A. 61*, 748−755.
2. Schuller, D. J., Wilks, A., Ortiz de Montellano, P. R., and Poulos, T. L. (1999) *Nat. Struct. Biol. 6*, 860−867.

3. Sugishima, M., Omata, Y., Kakuta, Y., Sakamoto, H., Noguchi, M., and Fukuyama, K. (2000) *FEBS Lett. 471*, 61−66.
4. Schuller, D. J., Zhu, W., Stojiljkovic, I., Wilks, A., and Poulos, T. L. (2001) *Biochemistry 40*, 11552−11558.
5. Sugishima, M., Sakamoto, H., Kakuta, Y., Omata, Y., Hayashi, S., Noguchi, M., and Fukuyama, K. (2002) *Biochemistry 41*, 7293−7300.
6. Maines, M. D. (1988) *FASEB J. 2*, 2557−2568.
7. Sugishima, M., Sakamoto, H., Higashimoto, Y., Omata, Y., Hayashi, S., Noguchi, M., and Fukuyama, K. (2002) *J. Biol. Chem. 277*, 45086−45090.
8. Yoshida, T., Noguchi, M., and Kikuchi, G. (1980) *J. Biochem. 88*, 557−563.
9. Collman, J. P., Brauman, J. I., Iverson, B. L., Sessler, J. L., Morris, R. M., and Gibson, Q. H. (1983) *J. Am. Chem. Soc. 105*, 3052−3064.
10. Springer, B. A., Sliger, S. G., Olson, J. S., and Phillips, G. N., Jr. (1994) *Chem. Rev. 94*, 699−714.
11. Vojtěchovský, J., Chu, K., Berendzen, J., Sweet, R. M., and Schlichting, I. (1999) *Biophys. J. 77*, 2153−2174.
12. Phillips, S. E., and Schoenborn, B. P. (1981) *Nature 292*, 81−82.
13. Cheng, X. D., and Schoenborn, B. P. (1991) *J. Mol. Biol. 220*, 381−399.
14. Li, T., Quillin, M. L., Phillips, G. N., Jr., and Olson, J. S. (1994) *Biochemistry 33*, 1433−1446.
15. Bhattacharya, S., Sukits, S. F., MacLaughlin, K. L., and Lecomte, J. T. (1997) *Biophys. J. 73*, 3230−3240.
16. Phillips, G. N., Jr., Teodoro, M. L., Li, T., Smith, B., and Olson, J. S. (1999) *J. Phys. Chem. B 103*, 8817−8829.
17. Migita, C. T., Matera, K. M., Ikeda-Saito, M., Olson, J. S., Fujii, H., Yoshimura, T., Zhou, H., and Yoshida, T. (1998) *J. Biol. Chem. 273*, 945−949.
18. Fujii, H., Dou, Y., Zhou, H., Yoshida, T., and Ikeda-Saito, M. (1998) *J. Am. Chem. Soc. 120*, 8251−8252.
19. Tenhunen, R., Marver, H. S., and Schmid, R. (1969) *J. Biol. Chem. 244*, 6388−6394.
20. Hidaka, T., Omata, Y., and Noguchi, M. (1996) *Kurume Med. J. 43*, 313−324.
21. Omata, Y., Asada, S., Sakamoto, H., Fukuyama, K., and Noguchi, M. (1998) *Acta Crystallogr. D54*, 1017−1019.
22. Leslie, A. G. W. (1992) *Joint CCP4 and ESF-EAMCB Newsletter on Protein Crystallography*, No. 26, Daresbury Laboratory, Warrington, U.K.
23. Collaborative Computational Project No. 4 (1994) *Acta Crystallogr. D50*, 760−763.
24. Kabsch, W. (1988) *J. Appl. Crystallogr. 21*, 916−924.
25. Otwinowski, Z., and Minor, W. (1997) *Methods Enzymol. 276*, 307−326.
26. McRee, D. E. (1992) *J. Mol. Graphics 10*, 44−47.
27. Brünger, A. T., Adams, P. D., Clore, G. M., DeLano, W. L., Gros, P., Grosse-Kunstleve, R. W., Jiang, J. S., Kuszewski, J., Nilges, N., Pannu, N. S., Read, R. J., Rice, L. M., Simonson, T., and Warren, G. L. (1998) *Acta Crystallogr. D54*, 905−921.
28. Laskowski, R. A., MacArthur, M. W., Moss, D. S., and Thornton, J. M. (1993) *J. Appl. Crystallogr. 26*, 283−291.
29. Sun, J., Wilks, A., Ortiz de Montellano, P. R., and Loehr, T. M. (1993) *Biochemistry 32*, 14151−14157.
30. Takahashi, S., Wang, J., Rousseau, D. L., Ishikawa, K., Yoshida, T., Takeuchi, N., and Ikeda-Saito, M. (1994) *Biochemistry 33*, 5531−5538.
31. Hawkins, B. K., Wilks, A., Powers, L. S., Ortiz de Montellano, P. R., and Dawson, J. H. (1996) *Biochim. Biophys. Acta 1295*, 165−173.
32. Lightning, L. K., Huang, H., Moenne-Loccoz, P., Loehr, T. M., Schuller, D. J., Poulos, T. L., and Ortiz de Montellano, P. R. (2001) *J. Biol. Chem. 276*, 10612−10619.
33. Fujii, H., Zhang, X., Tomita, T., Ikeda-Saito, M., and Yoshida, T. (2001) *J. Am. Chem. Soc. 123*, 6475−6484.
34. La Mar, G. N., Asokan, A., Espiritu, B., Yeh, D. C., Auclair, K., and Ortiz de Montellano, P. R. (2001) *J. Biol. Chem. 276*, 15676−15687.
35. Brucker, E. A., Olson, J. S., Ikeda-Saito, M., and Phillips, G. N., Jr. (1998) *Proteins 30*, 352−356.
36. Royer, W. E., Jr., Hendrickson, W. A., and Chiancone, E. (1990) *Science 249*, 518−521.
37. Li, Y., Syvitski, R. T., Auclair, K., Wilks, A., Ortiz de Montellano, P. R., and La Mar, G. N. (2002) *J. Biol. Chem. 277*, 33018−33031.
38. Enemark, J. H., and Feltham, R. D. (1974) *Coord. Chem. Rev. 13*, 339−406.
39. Scheidt, W. R., and Ellison, M. K. (1999) *Acc. Chem. Res. 32*, 350−359.
40. Takahashi, S., Ishikawa, K., Takeuchi, N., Ikeda-Saito, M., Yoshida, T., and Rousseau, D. L. (1995) *J. Am. Chem. Soc. 117*, 6002−6006.
41. Momenteau, M., and Reed, C. A. (1994) *Chem. Rev. 94*, 659−698.
42. Wang, J., Lu, S., Moenne-Loccoz, P., and Oritz de Montellano, P. R. (2003) *J. Biol. Chem. 278*, 2341−2347.
43. Moore, E. G., and Gibson, Q. H. (1976) *J. Biol. Chem. 251*, 2788−2794.
44. Hoshino, M., Laverman, L., and Ford, P. C. (1999) *Coord. Chem. Rev. 187*, 75−102.
45. Kraulis, P. J. (1991) *J. Appl. Crystallogr. 24*, 946−950.
46. Merritt, E. A., and Bacon, D. J. (1997) *Methods Enzymol. 277*, 505−524.
47. Lawrence, M. C., and Bourke, P. (2000) *J. Appl. Crystallogr. 33*, 990−991.

BI027268I